Advances in Geo-Energy Research

Vol. 21, No. 3, p. 220-237, 2026

Original article

Coupled simulation of pressure and saturation in water flooding using a quantum linear system solver

Li Xu[1,2], Yahong Xiang[1], Ming Li[2], Lei Zhang[3]*, Cunqi Jia[1]*

[1]*Physical Science and Engineering Division, King Abdullah University of Science and Technology, Thuwal 23955-6900, Saudi Arabia*

[2]*College of Science, China University of Petroleum (East China), Qingdao 266580, P. R. China*

[3]*State Key Laboratory of Deep Oil and Gas, China University of Petroleum (East China), Qingdao 266580, P. R. China*

Keywords:
Reservoir simulation
water flooding
implicit pressure explicit saturation
quantum linear solver
Harrow-Hassidim-Lloyd algorithm
statevector simulation

Cited as:
Xu, L., Xiang, Y., Li, M., Zhang, L., Jia, C. Coupled simulation of pressure and saturation in water flooding using a quantum linear system solver. Advances in Geo-Energy Research, 2026, 21(3): 220-237.
https://doi.org/10.46690/ager.2026.09.03

Abstract:
Sequential water flood simulation alternates implicit pressure solves with explicit saturation updates. This study examines, under ideal statevector access, how a solution state produced by the Harrow-Hassidim-Lloyd quantum linear system algorithm can be inserted into that sequential workflow for a two-phase model in one dimension. The evolving pressure systems are preconditioned from the left using rebuilt sparse approximate inverses, converted by Hermitian block dilation, and treated with signed phase estimation at finite resolution. The formulation also identifies the classical normalization, sign recovery, and complete field readout operations required before a solution state can drive the transport update. Steady and transient component tests precede coupled calculations on three successively refined grids. Across these grids, the statevector and direct pressure solutions remain closely aligned in direction, while the finest grid saturation trajectories show the largest difference and the statevector branch reaches the imposed upper saturation bound. Each plotted statevector pressure is aligned by a global scalar with the exact solution of its current dilated system, so the results assess algebraic data exchange rather than an independent reconstruction of physical pressure. A separate pilot covering five steps finds similar directional agreement between pressure solutions when a right sparse approximate inverse is rebuilt or updated using a sparse approximate map, but the combined setup and update time for recycling is markedly longer than the rebuilding time for this small problem. The results show that close directional agreement between pressure solutions does not by itself guarantee accurate saturation transport and thus provide a reference point for assessing such solvers in sequential reservoir simulation. All calculations use ideal statevectors; no quantum hardware, speedup of the complete workflow, or hardware advantage is demonstrated.

1. Introduction

Reservoir simulation is an essential tool in modern petroleum engineering (Peaceman, 1977; Aziz and Settari, 1979; Mattax and Dalton, 1990; Gerritsen and Durlofsky, 2005). It combines geological descriptions, rock and fluid properties, well controls, and recovery mechanisms within discretized conservation laws to forecast reservoir behavior. The resulting models support field development planning, production optimization, history matching, uncertainty quantification, and the comparison of alternative recovery strategies (Wan et al., 2024; Liu and Jia, 2026). These activities rarely rely on a single realization: studies of different operating conditions and ensemble workflows can require many forward simulations (van Essen et al., 2009). As the spatial resolution and physical detail of the models increase, computational

Yandy Scientific Press

*Corresponding author.
E-mail address: xuli@pku.edu.cn (L. Xu); yahong.xiang@kaust.edu.sa (Y. Xiang); liming@upc.edu.cn (M. Li); zhlei84@163.com (L. Zhang); cunqi.jia@kaust.edu.sa (C. Jia).

2207-9963 © The Author(s) 2026.

Received June 21, 2026; revised July 23, 2026; accepted August 6; available online August 10, 2026.

efficiency becomes a practical constraint (Li et al., 2019; Zhao et al., 2024; Hui et al., 2025). A substantial share of the computational cost arises from repeatedly solving the large sparse linear systems generated by the flow equations, particularly the global pressure system (Nardean et al., 2022; Meng et al., 2025). The reliability and cost of the pressure solver are integral to the usefulness of a reservoir simulator.

Water flooding illustrates how this computational requirement affects reservoir management decisions. It is a widely used secondary recovery process in which water is injected to replace produced fluids, support reservoir pressure, and displace mobile oil toward production wells (Dake, 1978; Willhite, 1986; Lake, 1989; Zhang et al., 2024). Its performance depends on the spatial distribution of permeability and porosity, phase viscosities, relative permeabilities, residual saturations, and the imposed well controls (Ertekin et al., 2001). Together, these factors govern pressure communication, mobility contrast, areal and vertical sweep, water front propagation, and the timing of water breakthrough. Pore scale imaging and simulation resolve the displacement mechanisms behind these averaged properties (Chen et al., 2022; Yang et al., 2023; Cai et al., 2024; Zou et al., 2024). Numerical water flood models are widely used to evaluate injection and production strategies and to forecast pressure, saturation, water cut, and production responses (Liu et al., 2021; Bai et al., 2022; He et al., 2023; Qin et al., 2024). Capturing these quantities requires a coupled description of flow driven by pressure and of phase transport rather than an isolated pressure calculation.

Among the standard formulations for two-phase reservoir simulation, the implicit pressure explicit saturation (IMPES) method represents this coupling by solving pressure implicitly and then updating saturation explicitly (Coats, 2000; El-Amin et al., 2017; Chen and Sun, 2021; Wang et al., 2025). Recent schemes for this class of problems emphasize energy stability and bounds preservation (Kou et al., 2022, 2023, 2024), together with phase wise conservative and homogenization based formulations (Chen et al., 2019; Fan et al., 2020). The pressure equation is solved implicitly to establish the global hydraulic response to injection, production, and boundary conditions, whereas water saturation is advanced explicitly from the resulting phase fluxes. At time step n, the current saturation $\boldsymbol{S}_w^n$ determines the relative permeabilities and mobilities and hence the pressure system $A_n \boldsymbol{p}^{n+1} = \boldsymbol{b}_n$. The recovered pressure determines the fluxes used to obtain $\boldsymbol{S}_w^{n+1}$, and the updated saturation then changes the coefficients of the next pressure system. This coupling generates an evolving sequence of pressure solves rather than a single isolated linear problem (Pacheco et al., 2017).

The pressure stage of this sequence defines the solver interface considered in this study. In generic notation, each solve takes the form:

$$G\boldsymbol{x} = \boldsymbol{d} \tag{1}$$

where G is the coefficient matrix, $\boldsymbol{x}$ is the unknown field, and $\boldsymbol{d}$ is the right side. Sparse direct solvers provide robustness, but factorization cost and matrix fill can restrict their use as reservoir systems grow. Large models are commonly treated with preconditioned iterative solvers whose convergence depends strongly on coefficient contrast, pressure block treatment, and preconditioner setup (Nardean et al., 2022). Practical implementations combine techniques such as incomplete factorization, algebraic multigrid, domain decomposition, and multistage preconditioning built around the pressure block to balance memory use, convergence, and parallel scalability (Nardean et al., 2022; Evstigneev et al., 2023; Nardean et al., 2024; Meng et al., 2025). The setup and update costs of these preconditioners remain relevant when a long sequence of related systems must be solved. Recent reservoir simulation studies have developed adaptive setup strategies for evolving multiphase systems (Zhao et al., 2022). Consecutive IMPES matrices are often closely related through their mobility updates, making these sequences a natural setting for reusing preconditioning information.

Against this classical background, the IMPES partition provides a natural hybrid quantum and classical decomposition: constitutive evaluations and saturation transport can remain classical, while the repeated pressure solve is treated as a quantum linear system subproblem. The quantum linear system algorithm introduced by Harrow, Hassidim, and Lloyd (HHL) is a candidate solver for this subproblem. For sparse, well-conditioned systems with efficient input access and limited output requirements, its ideal complexity can depend polylogarithmically on the matrix dimension, while retaining explicit dependence on sparsity, conditioning, and target accuracy (Harrow et al., 2009; Childs et al., 2017; Wossnig et al., 2018; Morales et al., 2026). HHL, however, returns a normalized quantum state proportional to the solution rather than a complete classical vector. Since the implemented IMPES flux form requires the reconstructed pressure values, the classical solution must be recovered from the solution state with the appropriate scale and sign (Henderson et al., 2024; Yalovetzky et al., 2024). The ideal statevector setting adopted here provides direct access to the simulated amplitudes, which isolates this algebraic reconstruction from sampling and hardware noise effects. The implemented saturation update uses the complete reconstructed pressure vector. This study evaluates the algebraic coupling enabled by direct access to statevector amplitudes rather than the complexity of the complete quantum workflow (Aaronson, 2015). Direct access to all amplitudes is a simulator operation, not a quantum hardware readout protocol. Recovering a complete pressure field or the corresponding fluxes across $O(N)$ faces on hardware would introduce measurement costs that depend on the output size and required precision, in addition to state preparation, matrix access, and postselection.

A further interface requirement is algebraic compatibility. Standard boundary treatments and discretizations scaled by rows can make an IMPES pressure matrix real and nonsymmetric, whereas the original HHL formulation assumes a Hermitian operator. Normal equations restore Hermiticity but square the 2-norm condition number; Hermitian block dilation doubles the dimension while retaining the singular value conditioning of the original operator. Finite quantum phase estimation (QPE) must also resolve small eigenvalue magnitudes and distinguish eigenvalue signs. Hermitian re-

formulation, preconditioning, phase resolution policy, and classical recovery must be designed as connected parts of the interface between HHL and IMPES (Clader et al., 2013; Bravo-Prieto et al., 2023; Morales et al., 2026).

Related quantum studies have considered Poisson, diffusion, Hele-Shaw, and incompressible flow problems (Cao et al., 2013; Meena et al., 2024; Ghafourpour and Laizet, 2025; Shayegan, 2026), as well as other quantum fluid simulation formulations (Gaitan, 2020; Chen et al., 2024; Xu et al., 2025). In the subsurface setting, preconditioning compatible with quantum algorithms, geologic fracture networks, state preparation, and information extraction have also been investigated (Golden et al., 2022; Henderson et al., 2023; Henderson et al., 2024). Taken together, these studies establish the relevance of quantum linear solvers to flow problems and motivate their examination within a sequential workflow for reservoir simulation. In the IMPES setting considered here, this examination is carried out through a closed interface between successive time steps: each reconstructed pressure approximation advances the saturation and thereby defines the next pressure system. This study develops and assesses the coupled interface using ideal statevector simulation.

Reported quantum linear solver studies mostly examine a single system, or a fixed matrix with changing right sides. A sequential reservoir workflow differs: the matrix, the right side and the spectrum are reassembled at every step from the updated saturation, so solver behavior and transport propagation cannot be assessed separately.

The contributions of this study are threefold. First, an interface between HHL and IMPES is formulated for an evolving water flooding problem in one dimension, in which HHL treats the implicit pressure solve while saturation transport remains classical. Second, nonsymmetric pressure systems after preconditioning from the left are accommodated through Hermitian block dilation and signed phase decoding at finite resolution; the framework specifies the operations required to recover the scale and sign before the lower block is supplied as the pressure approximation to the saturation update. Third, a staged numerical assessment connects canonical Poisson, diffusion, and advection benchmarks to the coupled water flooding problem and examines grid size sensitivity under a matched phase register policy. The assessment also includes a separate pilot covering five steps that compares a rebuilt right sparse approximate inverse (SPAI) with sparse approximate map (SAM) recycling (Chow and Saad, 1998; Saad, 2003; Carr et al., 2021).

The remainder of the paper is organized as follows. Section 2 establishes the HHL framework used throughout the study, including solution state recovery, preconditioning, Hermitian reformulation, and signed QPE at finite resolution. Section 3 presents the water flooding model in one dimension, its IMPES discretization, and the procedure coupling HHL with IMPES. Section 4 reports the component benchmark results and the water flooding results, and Section 5 summarizes the principal findings.

2. HHL framework for structured linear systems

This section introduces the HHL components used throughout the study: normalized solution state representation and scale recovery, finite QPE filtering, and Hermitian reformulations for systems that are not Hermitian. The advection benchmark uses normal equations, whereas the coupled water flooding calculations apply left preconditioning followed by Hermitian block dilation. Right preconditioning is retained for the separate SPAI/SAM recycling pilot.

2.1 Representation of the solution state and finite phase resolution

Using the notation of Eq. (1), first suppose that $G \in \mathbb{C}^{N_G \times N_G}$ is nonsingular and Hermitian, $\boldsymbol{x} \in \mathbb{C}^{N_G}$ is unknown, and $\boldsymbol{d} \in \mathbb{C}^{N_G} \setminus \{\mathbf{0}\}$ is known. In Dirac notation, a ket $|\psi\rangle$ is a column vector representing a quantum state, and the corresponding bra $\langle\psi|$ is its conjugate transpose. A qubit is a two-level quantum system, and an n_s-qubit system register spans 2^{n_s} computational basis states $|i\rangle$. This representation requires $n_s = \lceil \log_2 N_G \rceil$ system qubits. All matrices used in the reported numerical experiments have power-of-two dimensions; otherwise, the unused basis states would require a nonsingular padded extension.

The right side is supplied to HHL through amplitude encoding:

$$|d\rangle = \frac{1}{\|\boldsymbol{d}\|_2} \sum_{i=0}^{N_G-1} d_i |i\rangle \tag{2}$$

where d_i is the ith entry of $\boldsymbol{d}$ and $\|\cdot\|_2$ is the Euclidean vector norm. For matrices, $\|\cdot\|_2$ is the spectral norm and $\kappa_2(G) = \|G\|_2 \|G^{-1}\|_2$ is the 2-norm condition number.

Let λ_j and $|v_j\rangle$ be the jth eigenvalue and the corresponding orthonormal eigenvector of G, and let $\beta_j = \langle v_j | d \rangle$ be the coefficient of $|d\rangle$ in this eigenbasis. Then:

$$G = \sum_j \lambda_j |v_j\rangle\langle v_j| \tag{3}$$

$$|d\rangle = \sum_j \beta_j |v_j\rangle \tag{4}$$

$$G^{-1}|d\rangle = \sum_j \frac{\beta_j}{\lambda_j} |v_j\rangle \tag{5}$$

HHL leaves the eigenvectors unchanged while applying reciprocal eigenvalue weights to their amplitudes.

QPE is applied to $U = \exp(\mathrm{i}G\tau)$, where $\mathrm{i} = \sqrt{-1}$ and $\tau > 0$ is an evolution time selected from a known spectral bound. The jth eigenphase is:

$$\varphi_j = \frac{\lambda_j \tau}{2\pi} \pmod 1 \tag{6}$$

The mapping from λ_j to φ_j must be unique on the relevant spectrum. For a positive spectrum it is sufficient to choose $0 < \lambda_j \tau < 2\pi$ for every j; for a signed spectrum, the convention $|\lambda_j|\tau < \pi$ permits decoding in the interval $[-1/2, 1/2)$. With n_p phase qubits, QPE has $N_b = 2^{n_p}$ phase bins and nominal eigenvalue spacing:

$$\Delta\lambda = \frac{2\pi}{\tau N_b} \tag{7}$$

In the resolved eigenphase limit, QPE records the bin corresponding to each relevant eigenphase, after which a controlled ancilla rotation applies the reciprocal weight (Harrow et al., 2009):

$$\theta_j = 2\arcsin\left(\frac{C}{\lambda_j}\right), \qquad 0 < C \le \min_j |\lambda_j| \tag{8}$$

where C is a positive scaling constant that makes every rotation well defined. After inverse QPE, selecting the ancilla in $|1\rangle$ gives:

$$|x\rangle = \frac{G^{-1}|d\rangle}{\|G^{-1}|d\rangle\|_2} \tag{9}$$

in the exact QPE limit, with postselection probability:

$$P_1 = C^2 \sum_j \frac{|\beta_j|^2}{|\lambda_j|^2} = C^2 \|G^{-1}|d\rangle\|_2^2 \tag{10}$$

The relation $G^{-1}|d\rangle = \boldsymbol{x}/\|\boldsymbol{d}\|_2$ gives the corresponding classical solution norm:

$$\|\boldsymbol{x}\|_2 = \frac{\|\boldsymbol{d}\|_2\sqrt{P_1}}{C} \tag{11}$$

in the same limit. In this ideal limit, HHL returns a normalized solution direction, while the corresponding postselection probability supplies the scale needed to recover the classical norm. Without amplitude amplification, one accepted sample requires $1/P_1$ executions on average; P_1 is a sampling cost indicator rather than an accuracy metric.

With finite n_p, eigenmode j is distributed among phase bins m with QPE amplitudes a_{jm}, where $\sum_m |a_{jm}|^2 = 1$. Let $r(m)$ be the reciprocal assigned to bin m, with $r(m) = 0$ for a discarded bin, and choose $C > 0$ such that $|Cr(m)| \le 1$ for every phase bin. The corresponding controlled ancilla amplitude is $Cr(m)$. Inverse QPE does not generally return the phase register exactly to $|0\rangle$, so the successful event used here is defined jointly by ancilla state $|1\rangle$ and phase state $|0\rangle$. The resulting unnormalized system state and its probability are:

$$|\Psi_1^{(n_p)}\rangle_s = C\sum_j \beta_j \Phi_j^{(n_p)} |v_j\rangle_s \tag{12}$$

$$\Phi_j^{(n_p)} = \sum_{m=0}^{N_b-1} |a_{jm}|^2 r(m) \tag{13}$$

$$P_1^{(n_p)} = \left\||\Psi_1^{(n_p)}\rangle_s\right\|_2^2 = C^2 \sum_j |\beta_j \Phi_j^{(n_p)}|^2 \tag{14}$$

where the subscript s denotes the system register and $\Phi_j^{(n_p)}$ is the effective reciprocal filter. The probability weight $|a_{jm}|^2$ results from applying QPE and its adjoint. If $\boldsymbol{v}_j$ denotes the classical column vector representation of $|v_j\rangle$, the corresponding finite register approximation and its scale satisfy:

$$\widetilde{\boldsymbol{x}}^{(n_p)} = \|\boldsymbol{d}\|_2 \sum_j \beta_j \Phi_j^{(n_p)} \boldsymbol{v}_j \tag{15}$$

$$\|\widetilde{\boldsymbol{x}}^{(n_p)}\|_2 = \frac{\|\boldsymbol{d}\|_2\sqrt{P_1^{(n_p)}}}{C} \tag{16}$$

For a fixed Hermitian linear system, the finite register error relative to the exact inverse can be written as:

$$\left\|\widetilde{\boldsymbol{x}}^{(n_p)} - \boldsymbol{x}\right\|_2 = \|\boldsymbol{d}\|_2 \left(\sum_j |\beta_j|^2 \left|\Phi_j^{(n_p)} - \lambda_j^{-1}\right|^2\right)^{1/2} \tag{17}$$

Phase bin leakage, reciprocal truncation, and finite bin spacing can alter both the direction and the norm of the recovered solution. Increasing n_p reduces the nominal bin spacing, but does not by itself guarantee monotonic error reduction when appreciable spectral weight lies near a cutoff or between available phase bins.

HHL with a finite register implements an approximate spectral inverse. When every occupied eigenphase is exactly resolved in a retained bin m_j with $r(m_j) = 1/\lambda_j$, then $\Phi_j^{(n_p)} = 1/\lambda_j$, $|\Psi_1^{(n_p)}\rangle_s = CG^{-1}|d\rangle$, and $P_1^{(n_p)} = P_1$. After normalization, the conditional system state is Eq. (9), while $\widetilde{\boldsymbol{x}}^{(n_p)} = \boldsymbol{x}$ and Eq. (15) becomes Eq. (11). Even after this scale recovery, the global phase of an isolated quantum state is unobservable. Reconstructing a real-valued solution therefore requires an external sign convention, while recovering all vector entries requires a separate readout procedure. On quantum hardware, direct access to statevector amplitudes would have to be replaced by tomography or by a measurement procedure designed for the application. The flux form IMPES update requires either the N pressure entries or an equivalent set of $O(N)$ face fluxes, so producing a complete classical field already incurs a cost that grows with the output size. Further sampling is required to achieve the target precision. Without amplitude amplification, a jointly accepted output requires $1/P_1$ circuit executions on average. If the joint event is estimated from N_e Bernoulli trials, the relative standard deviation of the recovered scale, which is proportional to $\sqrt{P_1}$, is approximately:

$$\frac{1}{2}\sqrt{\frac{1-P_1}{N_e P_1}} \tag{18}$$

A target relative scale precision ε_s therefore requires $N_e \simeq (1-P_1)/(4P_1\varepsilon_s^2)$ executions solely to estimate the postselection probability. State preparation, implementation of the matrix exponential or an equivalent block encoding, and pressure or flux readout add further costs. These operations are excluded from the ideal statevector calculations reported here.

The corresponding circuit sequence in the resolved QPE limit, from encoding of the right side and phase estimation to the controlled reciprocal rotation, inverse QPE, and postselection, is summarized in Fig. 1.

2.2 Hermitian reformulations and preconditioning

For a nonsingular matrix G that is not Hermitian, let $G^\dagger$ denote its conjugate transpose. The normal equations are:

$$G^\dagger G\boldsymbol{x} = G^\dagger \boldsymbol{d} \tag{19}$$

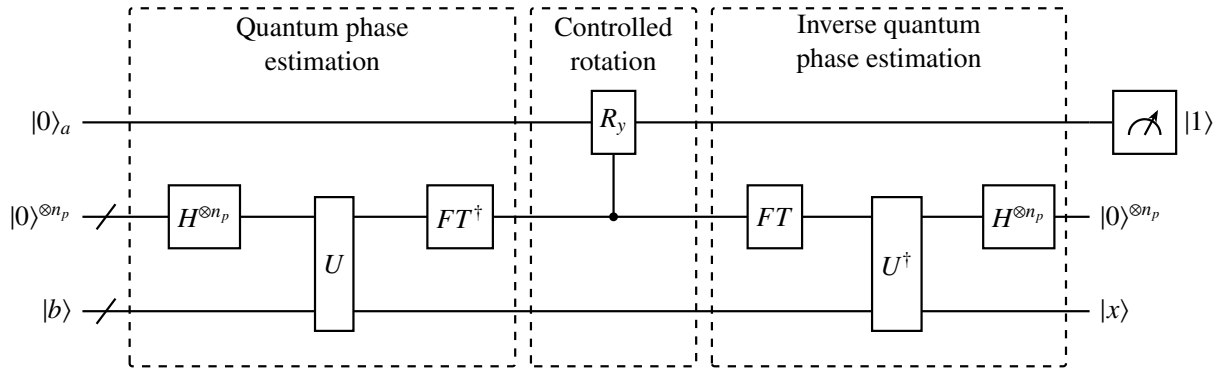


Fig. 1. Standard HHL sequence in the resolved QPE limit; $|b\rangle$ denotes $|d\rangle$. The finite QPE calculations also condition on the phase register being in $|0\rangle^{\otimes n_p}$.

$$\kappa_2(G^\dagger G) = \kappa_2(G)^2 \tag{20}$$

They preserve the exact solution but square the 2-norm condition number and can increase matrix access and right side preparation costs. The advection benchmark in Part I of Section 4 adopts this route, whereas the water flooding formulation uses Hermitian block dilation.

Hermitian conversion supplies the operator required by the HHL construction used here, whereas preconditioning controls conditioning and the cost of repeated solves. The coupled water flooding calculations use a nonsingular left preconditioner W, for which:

$$WG\boldsymbol{x} = W\boldsymbol{d} \tag{21}$$

The unknown remains $\boldsymbol{x}$, while both the matrix and right side are multiplied from the left before Hermitian block dilation. The lower solution block represents $\boldsymbol{x}$ directly.

For comparison, a separate SPAI/SAM pilot covering five steps uses right preconditioning. A nonsingular right preconditioner P defines:

$$GP\boldsymbol{y} = \boldsymbol{d} \tag{22}$$

$$\boldsymbol{x} = P\boldsymbol{y} \tag{23}$$

The successful doubled register state for this system, which is preconditioned from the right, has a lower block proportional to the finite QPE approximation to $\boldsymbol{y}$, which would then be mapped through P classically.

A right SPAI at a reference step r is defined by (Chow and Saad, 1998; Saad, 2003):

$$P_r = \arg\min_{P\in\mathcal{S}_P} \|G_rP - I\|_F \tag{24}$$

where G_r is the reference matrix, I is the identity matrix of compatible dimension, $\mathcal{S}_P$ is a prescribed sparsity pattern, and $\|\cdot\|_F$ denotes the Frobenius norm. For a later matrix G_n, a sparse approximate map (SAM) updates the reference preconditioner (Carr et al., 2021):

$$N_n = \arg\min_{N\in\mathcal{S}_N} \|G_nN - G_r\|_F \tag{25}$$

$$P_n = N_nP_r \tag{26}$$

where $\mathcal{S}_N$ is the prescribed sparsity pattern of the map. The difference between the preconditioned operators satisfies:

$$\begin{aligned}\|G_nP_n - G_rP_r\|_F &= \|(G_nN_n - G_r)P_r\|_F \\ &\le \|G_nN_n - G_r\|_F\|P_r\|_2\end{aligned} \tag{27}$$

Eq. (27) shows that a small SAM residual provides an algebraic basis for recycling P_r, subject to its amplification by $\|P_r\|_2$. Both SPAI construction and SAM updating involve classical sparse least-squares problems. The independently rebuilt SPAI and SAM recycling paths are compared in Section 4.2. Even if P_r and N_n are individually restricted to tridiagonal patterns, their product $P_n = N_nP_r$ generally has a wider band. No numerical claim about the sparsity of the final block encoding is inferred from the nominal factor patterns alone. The retained record of the original pilot covering five steps does not include counts of nonzero entries in the products or a numerical drop tolerance setting.

To describe the subsequent Hermitian conversion, let $M\boldsymbol{z} = \boldsymbol{d}$ denote the nonsingular system, which is generally not Hermitian, to be converted for HHL. Here, $M = G$ and $\boldsymbol{z} = \boldsymbol{x}$ without preconditioning, $M = WG$, $\boldsymbol{z} = \boldsymbol{x}$, and the right side is $W\boldsymbol{d}$ after left preconditioning, whereas $M = GP$ and $\boldsymbol{z} = \boldsymbol{y}$ after right preconditioning. Instead of forming normal equations, one may use the Hermitian block dilation:

$$\mathscr{H}(M) = \begin{pmatrix} 0 & M \\ M^\dagger & 0 \end{pmatrix} \tag{28}$$

$$\mathscr{H}(M)\begin{pmatrix} 0 \\ \boldsymbol{z} \end{pmatrix} = \begin{pmatrix} \boldsymbol{d} \\ 0 \end{pmatrix} \tag{29}$$

Its eigenvalues are $\pm\sigma_j(M)$, where $\sigma_j(M) > 0$ are the singular values of M. The relation $\kappa_2(\mathscr{H}(M)) = \kappa_2(M)$ holds, although the dimension is doubled. Both spectral signs must be retained. For $\rho > 2\|\mathscr{H}(M)\|_2$, QPE applied to $U = \exp(\mathrm{i}\mathscr{H}(M)\tau)$ with $\tau = 2\pi/\rho$ decodes the phase bin index $m \in \{0,\ldots,N_b-1\}$ as:

$$\ell_b(m)=\begin{cases} m, & m<\dfrac{N_b}{2} \\ m-N_b, & m\geq\dfrac{N_b}{2} \end{cases}, \qquad \widehat{\lambda}(m)=\frac{\rho}{N_b}\ell_b(m) \tag{30}$$

The resulting eigenvalue spacing is $\Delta\lambda=\rho/N_b$.

To avoid inversion of the zero or unresolved spectrum, introduce a cutoff $\lambda_c>0$ and retain the bin set:

$$\mathscr{M}_r=\left\{m:\ |\widehat{\lambda}(m)|\geq\lambda_c\right\} \tag{31}$$

The reciprocal lookup in Eq. (12) is:

$$r(m)=\begin{cases} \dfrac{1}{\widehat{\lambda}(m)}, & m\in\mathscr{M}_r \\ 0, & m\notin\mathscr{M}_r \end{cases} \tag{32}$$

The cutoff discards the zero bin. For bins that are not paired with themselves, $r((-m) \bmod N_b)=-r(m)$. If $q_m(\lambda)=|a_m(\lambda)|^2$ denotes the QPE probability for eigenvalue λ, the signed phase convention gives $q_m(-\lambda)=q_{(-m) \bmod N_b}(\lambda)$. Excluding the Nyquist bin, which is paired with itself, would make the scalar finite QPE filter $F_{n_p}(\lambda)=\sum_m q_m(\lambda)r(m)$ odd: $F_{n_p}(-\lambda)=-F_{n_p}(\lambda)$. It follows that $F_{n_p}(\mathscr{H}(M))$ is block off-diagonal, and applying it to $(\boldsymbol{d},\boldsymbol{0})^T$ produces only a lower block solution component. The reported lookup instead retains the Nyquist bin under the signed decoding in Eq. (30); at finite resolution, upper block leakage is therefore not ruled out algebraically, and only the extracted lower block is supplied to the pressure reconstruction. Assuming $\mathscr{M}_r\neq\varnothing$, choose:

$$\begin{gathered} 0<C\leq\min_{m\in\mathscr{M}_r}|\widehat{\lambda}(m)| \\ \theta(m)=2\arcsin\big(Cr(m)\big),\ 0\leq m<N_b \end{gathered} \tag{33}$$

The angle is zero for a discarded bin and negative for a retained negative eigenvalue. Replacing $r(m)$ by $1/|\widehat{\lambda}(m)|$ on retained bins would discard the eigenvalue signs and would not reproduce the required signed inverse action, even in the resolved eigenphase limit. Increasing n_p refines $\Delta\lambda$, but accuracy also depends on the cutoff and on spectral weight near zero.

After recovering the scale from the postselection probability and performing a full classical readout, a candidate solution can be assessed in the original system using the following residual:

$$R_o=\frac{\|G\boldsymbol{x}_q-\boldsymbol{d}\|_2}{\|\boldsymbol{d}\|_2} \tag{34}$$

where $\boldsymbol{x}_q$ is the recovered classical vector. For a real-valued problem, this residual may also be evaluated for the two possible global signs, with the sign giving the smaller residual retained. This provides a formal sign-selection rule after readout but is not used for the displayed coupled trajectories, which are aligned with the exact solution by a global scalar as described in Section 3.3.

The reported calculations use ideal statevectors, exhaustive reciprocal angle lookup, and direct amplitude access to examine the algebraic formulation and finite QPE behavior of the HHL solver (Harrow et al., 2009).

3. Formulation coupling HHL with IMPES for water flooding in one dimension

This section specializes the framework of Section 2 to immiscible water flooding in one dimension. After stating the physical model and its IMPES discretization, HHL is introduced at the stage where pressure is solved implicitly at each time step.

3.1 Physical model

One-dimensional displacement of oil by water is considered in a homogeneous porous core of length L and constant cross-sectional area A_c. The coordinate $x\in[0,L]$ increases from the inlet to the outlet, and t denotes time. Water and oil are assumed incompressible and immiscible; gravity and capillary pressure are neglected. For phase $\alpha\in\{w,o\}$, with w denoting water and o denoting oil, the interior equations without sources on $0<x<L$ are:

$$\phi\frac{\partial S_\alpha}{\partial t}+\frac{\partial u_\alpha}{\partial x}=0 \tag{35}$$

$$u_\alpha=-\Lambda_\alpha(S_w)\frac{\partial p}{\partial x} \tag{36}$$

where ϕ is porosity, $S_\alpha(x,t)$ is phase saturation, $u_\alpha(x,t)$ is Darcy velocity, $p(x,t)$ is the common pressure, and Λ_α is phase mobility. The two saturations and the mobilities satisfy:

$$S_w+S_o=1 \tag{37}$$

$$\Lambda_\alpha(S_w)=\frac{kk_{r\alpha}(S_w)}{\mu_\alpha} \tag{38}$$

$$\Lambda_t(S_w)=\Lambda_w(S_w)+\Lambda_o(S_w) \tag{39}$$

where k is absolute permeability, $k_{r\alpha}$ is relative permeability, μ_α is dynamic viscosity, and Λ_t is total mobility.

The relative permeabilities are represented by Corey curves (Dake, 1978; Lake, 1989):

$$S_e=\frac{S_w-S_{wc}}{1-S_{wc}-S_{or}} \tag{40}$$

$$k_{rw}=k_{rw}^0S_e^{\eta_w} \tag{41}$$

$$k_{ro}=k_{ro}^0(1-S_e)^{\eta_o} \tag{42}$$

where S_e is effective water saturation, S_{wc} is connate water saturation, S_{or} is residual oil saturation, k_{rw}^0 and k_{ro}^0 are endpoint relative permeabilities, and η_w and η_o are Corey exponents. The physical Corey interval is $S_{wc}\leq S_w\leq 1-S_{or}$.

The configuration with a prescribed rate uses the initial condition $S_w(x,0)=S_{wc}$, injects pure water at volumetric rate $Q_v>0$, and prescribes the outlet pressure p_L:

$$u_w(0,t)=\frac{Q_v}{A_c} \tag{43}$$

$$u_o(0,t)=0 \tag{44}$$

$$u_t(0,t)=\frac{Q_v}{A_c} \tag{45}$$

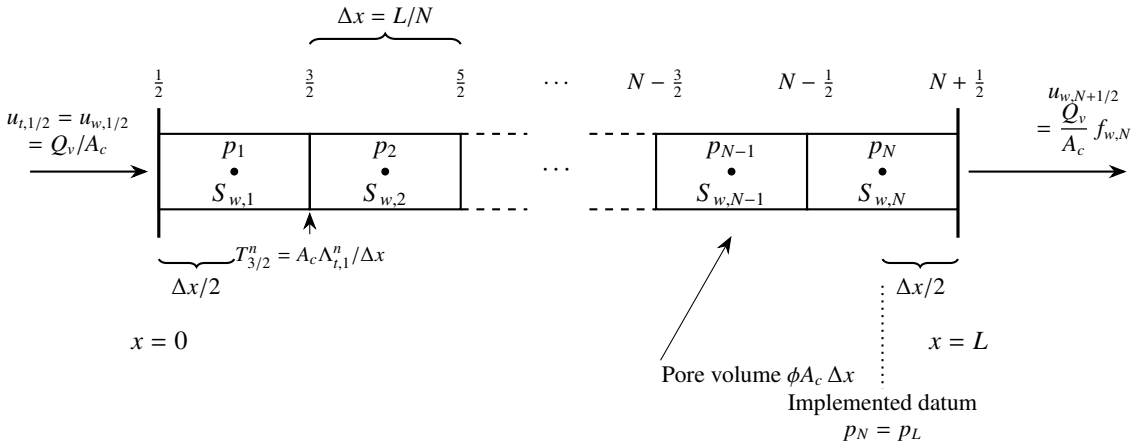


Fig. 2. Implemented collocated control volume layout and boundary treatment. The inlet rate is prescribed at face $1/2$, whereas p_L is assigned to the final cell centered pressure degree of freedom.

$$p(L,t) = p_L \tag{46}$$

where $u_t = u_w + u_o$. Adding the phase balances gives the interior pressure equation:

$$\frac{\partial}{\partial x}\left(\Lambda_t(S_w)\frac{\partial p}{\partial x}\right) = 0 \tag{47}$$

For this incompressible problem in one dimension, with no sources, gravity, or capillary pressure, the prescribed total rate makes the total velocity spatially constant:

$$u_t(x,t) = \frac{Q_v}{A_c} \tag{48}$$

It follows that:

$$u_w = f_w(S_w)u_t, \quad f_w(S_w) = \frac{\Lambda_w(S_w)}{\Lambda_t(S_w)} \tag{49}$$

and an exact pressure solve reduces the saturation equation to:

$$\phi\frac{\partial S_w}{\partial t} + q\frac{\partial f_w(S_w)}{\partial x} = 0 \tag{50}$$

The complete pressure vector is not mathematically required to advance saturation when the constant total flux is enforced exactly. The flux form based on pressure is retained here to examine the algebraic data exchange between the HHL statevector solver and the IMPES update. This simplified case tests data transfer between successive solver steps rather than establishing that full pressure reconstruction is physically essential.

No saturation value is prescribed at the outflow boundary; its water flux is closed by the local fractional flow in the discrete update below. Within IMPES, Λ_t is evaluated from S_w^n, pressure is solved implicitly, and water saturation is then advanced explicitly.

3.2 Implemented IMPES discretization

To connect the continuous model with the numerical experiments, this subsection presents the exact algebraic scheme used in the calculations. The interval is partitioned into N equal blocks of width $\Delta x = L/N$, with discrete entries indexed by $i = 1,\ldots,N$. The implemented algebraic scheme uses N cell-centered control volumes $\Omega_i = [(i-1)\Delta x, i\Delta x]$ with centers $x_i = (i-1/2)\Delta x$, and collocate the pressure p_i and water saturation $S_{w,i}$ at the same center (Fig. 2). This convention is consistent with the full width saturation storage and the flux indexing of the code. The pressure inlet row (Eq. (52)) enforces the prescribed total flux at the first internal face $3/2$, whereas the saturation update applies the inlet flux at boundary face $1/2$; incompressibility in the absence of sources makes the two fluxes equal. The outlet datum is assigned directly to the final cell centered unknown p_N, not through a half cell boundary face row. This is an N-block layout rather than a nodal grid that includes the endpoints and has $\Delta x = L/(N-1)$. For an exact fixed rate solve, replacing the assignment by the standard half cell row with the same one-sided mobility adds the uniform offset $(Q_v/A_c)\Delta x/(2\Lambda^n_{t,N})$ to all cell centered pressures and leaves the intercell gradients, phase fluxes, and direct saturation update unchanged. The altered pressure matrix can nevertheless change the finite QPE error and the resulting hybrid trajectory. At time step n, an IMPES update consists of two sequential operations.

Step 1: Implicit pressure solve. Given the discrete saturation vector $\boldsymbol{S}_w^n = (S_{w,1}^n,\ldots,S_{w,N}^n)^T$, define the cell values $\Lambda_{\gamma,i}^n = \Lambda_\gamma(S_{w,i}^n)$ for $\gamma \in \{w,o,t\}$, where $\gamma = t$ denotes total mobility. For $Q_v > 0$, the implemented flux between entries i and $i+1$ uses the left, upstream mobility:

$$u_{\alpha,i+1/2}^{n+1} = -\Lambda_{\alpha,i}^n\frac{p_{i+1}^{n+1} - p_i^{n+1}}{\Delta x}, \qquad \alpha \in \{w,o\} \tag{51}$$

Let $\boldsymbol{p}^{n+1} = (p_1^{n+1},\ldots,p_N^{n+1})^T$. The implemented pressure system $A_n\boldsymbol{p}^{n+1} = \boldsymbol{b}_n$ is:

$$p_1^{n+1} - p_2^{n+1} = \frac{\Delta x\, Q_v}{A_c\Lambda_{t,1}^n} \tag{52}$$

$$\Lambda_{t,i-1}^n p_{i-1}^{n+1} - (\Lambda_{t,i-1}^n + \Lambda_{t,i}^n)p_i^{n+1} + \Lambda_{t,i}^n p_{i+1}^{n+1} = 0, \quad 2 \le i \le N-1 \tag{53}$$

$$p_N^{n+1} = p_L \tag{54}$$

Equivalently:

$$A_n = \begin{pmatrix} 1 & -1 & & & \\ \Lambda^n_{t,1} & -(\Lambda^n_{t,1}+\Lambda^n_{t,2}) & \Lambda^n_{t,2} & & \\ & \ddots & \ddots & \ddots & \\ & & \Lambda^n_{t,N-2} & -(\Lambda^n_{t,N-2}+\Lambda^n_{t,N-1}) & \Lambda^n_{t,N-1} \\ & & & & 1 \end{pmatrix} \tag{55}$$

$$\boldsymbol{b}_n = \begin{pmatrix} \dfrac{\Delta x Q_v}{(A_c \Lambda^n_{t,1})} \\ 0 \\ \vdots \\ 0 \\ p_L \end{pmatrix} \tag{56}$$

The chosen inlet row normalization and direct enforcement of the outlet pressure make A_n nonsymmetric, although the underlying scalar elliptic operator is symmetric. This matrix form is retained because it is the algebraic system used in the reported calculations; all subsequent spectral settings and postselection probabilities therefore refer to this fixed row scaling.

The nonsymmetry of A_n is associated with this retained boundary row representation rather than with the underlying pressure operator. An equivalent symmetric formulation follows by eliminating $p_N^{n+1} = p_L$, defining $\widehat{\boldsymbol{p}}^{n+1} = (p_1^{n+1}, \ldots, p_{N-1}^{n+1})^T$, scaling the inlet equation by $\Lambda^n_{t,1}$, and reversing the signs of the interior balance equations:

$$K_n \widehat{\boldsymbol{p}}^{n+1} = \widehat{\boldsymbol{b}}_n \tag{57}$$

where:

$$K_n = \begin{pmatrix} \Lambda^n_{t,1} & -\Lambda^n_{t,1} & & & \\ -\Lambda^n_{t,1} & \Lambda^n_{t,1}+\Lambda^n_{t,2} & -\Lambda^n_{t,2} & & \\ & \ddots & \ddots & \ddots & \\ & & -\Lambda^n_{t,N-2} & \Lambda^n_{t,N-2}+\Lambda^n_{t,N-1} & \end{pmatrix} \tag{58}$$

$$\widehat{\boldsymbol{b}}_n = \begin{pmatrix} \dfrac{\Delta x Q_v}{A_c} & 0 & \cdots & \Lambda^n_{t,N-1} p_L \end{pmatrix}^T \tag{59}$$

For any nonzero $\xi \in \mathbb{R}^{N-1}$:

$$\xi^T K_n \xi = \sum_{i=1}^{N-2} \Lambda^n_{t,i} (\xi_i - \xi_{i+1})^2 + \Lambda^n_{t,N-1} \xi^2_{N-1} > 0 \tag{60}$$

provided the total mobilities are positive. This proves that K_n is symmetric positive definite and could be supplied directly to HHL. The Hermitian block dilation used below is required by the selected full boundary row representation and its preconditioned algebraic system; it should not be interpreted as evidence that the physical pressure operator is intrinsically non-Hermitian.

Step 2: Explicit saturation update. Using the recovered pressure $\boldsymbol{p}^{n+1}$ and the upstream flux in Eq. (51), the interior saturation entries are updated by:

$$S^{n+1}_{w,i} = S^n_{w,i} + \frac{\Delta t}{\phi \Delta x^2} \Big[\Lambda^n_{w,i} (p^{n+1}_{i+1} - p^{n+1}_i) - \Lambda^n_{w,i-1} (p^{n+1}_i - p^{n+1}_{i-1}) \Big], \; 2 \le i \le N-1 \tag{61}$$

where Δt is the time step. The implemented boundary updates are:

$$S^{n+1}_{w,1} = S^n_{w,1} + \frac{\Delta t}{\phi \Delta x} \left(\frac{Q_v}{A_c} - \Lambda^n_{w,1} \frac{p^{n+1}_1 - p^{n+1}_2}{\Delta x} \right) \tag{62}$$

$$S^{n+1}_{w,N} = S^n_{w,N} + \frac{\Delta t}{\phi \Delta x} \left(\Lambda^n_{w,N-1} \frac{p^{n+1}_{N-1} - p^{n+1}_N}{\Delta x} - \frac{Q_v}{A_c} f^n_{w,N} \right) \tag{63}$$

with fractional flow $f^n_{w,N} = \Lambda^n_{w,N} / (\Lambda^n_{w,N} + \Lambda^n_{o,N})$.

For the exact pressure update with a prescribed rate, define the advective Courant number:

$$\nu_N = \frac{Q_v \Delta t}{\phi A_c \Delta x_N} \tag{64}$$

The corresponding first-order upwind fractional flow scheme is monotone under the reference condition:

$$\nu_N \max_{S_w \in [S_{wc}, 1-S_{or}]} f'_w(S_w) \le 1 \tag{65}$$

The Corey tables used in the calculations are linearly interpolated from 50 uniformly spaced saturation values, and their maximum piecewise derivative is approximately 4.4934. With $\Delta t = 1$ s and $\Delta x_N = L/N$, the left side of Eq. (65) is approximately 0.0187, 0.0374, and 0.0749 for $N = 8$, 16, and 32, respectively. These values characterize the exact flux reference discretization; finite QPE flux perturbations require separate monitoring. In the reported implementation, both trajectories project each updated saturation onto $[S_{wc}, 1 - S_{or}]$. The upper bound is reached during part of the $N = 32$ statevector trajectory, so its bounded stored profile is partly imposed by this projection. Bounded profiles therefore do not, by themselves, establish stability of the unprojected update. No time step sweep is performed; the reported stability indicator refers to the chosen $\Delta t = 1$ s.

3.3 Coupling HHL to the IMPES pressure solver

In IMPES, constitutive evaluation and saturation advancement remain classical, whereas solving the global pressure equation is the repeated linear system task. HHL is introduced specifically for this task, and the recovered pressure is then supplied to the classical saturation update.

The coupled calculations for different grid sizes use a left SPAI. At time step n, the preconditioner is defined by:

$$W_n = \arg\min_{W \in \mathcal{S}_W} \|W A_n - I\|_F \tag{66}$$

where $\mathcal{S}_W$ is the tridiagonal row pattern used in the implementation, restricted at the boundary rows. The system after preconditioning from the left is:

$$\overline{A}_n \boldsymbol{p}^{n+1} = \overline{\boldsymbol{b}}_n \tag{67}$$

$$\overline{A}_n = W_n A_n \tag{68}$$

$$\overline{\boldsymbol{b}}_n = W_n \boldsymbol{b}_n \tag{69}$$

Provided that W_n is nonsingular, this system is equivalent to the original pressure equation. The matrix $\overline{A}_n$ is real and generally nonsymmetric, and its Hermitian block dilation is:

$$H_n = \begin{pmatrix} 0 & \overline{A}_n \\ \overline{A}_n^T & 0 \end{pmatrix} \tag{70}$$

$$H_n \begin{pmatrix} 0 \\ \boldsymbol{p}^{n+1} \end{pmatrix} = \begin{pmatrix} \overline{\boldsymbol{b}}_n \\ 0 \end{pmatrix} \tag{71}$$

The lower block represents pressure directly; no right preconditioner map is applied after extraction. Provided that $\overline{A}_n$ is nonsingular, the eigenvalues of H_n are $\pm\sigma_j(\overline{A}_n)$ and $\kappa_2(H_n) = \kappa_2(\overline{A}_n)$, so the dilation does not square the condition number. With $\mathscr{H}(\overline{A}_n) = H_n$, the circuit sequence in Fig. 1 uses the signed phase convention and truncated reciprocal construction of Eqs. (30)-(33). The statevector implementation evaluates an exhaustive table of angles for 2^{n_p} phase bins, with the zero bin angle set to zero. At each pressure step, the lookup parameters are:

$$\rho_n = 2.1\|H_n\|_2 \tag{72}$$

$$\tau_n = \frac{2\pi}{\rho_n} \tag{73}$$

$$\Delta\lambda_n = \frac{\rho_n}{2^{n_p}} \tag{74}$$

$$C_n = \frac{\rho_n}{2^{n_p+1}} = \frac{\Delta\lambda_n}{2} \tag{75}$$

The zero bin is not inverted, the signed Nyquist bin is retained, and $\lambda_{c,n} = C_n$. The relation $C_n/\Delta\lambda_n = 1/2$ ensures that every nonzero bin has a real rotation angle in Eq. (33), while the factor 2.1 enforces the strict condition $\rho_n > 2\|H_n\|_2$ that prevents phase wrapping. This rule also gives $\Delta\lambda_n/\|H_n\|_2 = 2.1/2^{n_p}$, so increasing n_p tests phase resolution under a fixed scaling policy. The exact spectral norm is evaluated classically in the present statevector calculations. For a larger sparse problem, the exact norm could be replaced by a computable upper bound $\zeta_n \geq \|H_n\|_2$, such as $\|H_n\|_F$ or $\sqrt{\|H_n\|_1\|H_n\|_\infty}$, with $\rho_n = 2.1\zeta_n$. This preserves the condition that prevents phase wrapping, but a loose bound increases the phase spacing and may require a larger phase register to maintain comparable resolution.

Let $\widehat{\boldsymbol{z}}_n$ denote the normalized statevector obtained after postselection. It is produced by the joint spectral filter in Eqs. (12)-(14); $P_{1,n}$ denotes the probability of the same joint ancilla-$|1\rangle$ and phase-$|0\rangle$ branch at step n. With normalized input $(\overline{\boldsymbol{b}}_n, 0)^T/\|\overline{\boldsymbol{b}}_n\|_2$, the formal reconstruction based on this probability is:

$$\widetilde{\boldsymbol{z}}_n = \frac{\|\overline{\boldsymbol{b}}_n\|_2\sqrt{P_{1,n}}}{C_n}\widehat{\boldsymbol{z}}_n \tag{76}$$

$$\widetilde{\boldsymbol{p}}^{n+1} = \mathrm{Re}(\Pi_\ell \widetilde{\boldsymbol{z}}_n) \tag{77}$$

where Π_ℓ extracts the lower block. In a formal reconstruction, the overall sign may then be selected using the residual of the original system in Eq. (34) after scale recovery and full classical readout. The present coupled profiles do not use these two recovery operations. Instead, the simulator evaluates the exact solution of the dilated system at the same time step:

$$\boldsymbol{z}_{*,n} = H_n^{-1}\begin{pmatrix} \overline{\boldsymbol{b}}_n \\ 0 \end{pmatrix} \tag{78}$$

$$\chi_n = \frac{\widehat{\boldsymbol{z}}_n^\dagger \boldsymbol{z}_{*,n}}{\widehat{\boldsymbol{z}}_n^\dagger \widehat{\boldsymbol{z}}_n} \tag{79}$$

$$\boldsymbol{p}_u^{n+1} = \mathrm{Re}[\Pi_\ell(\chi_n \widehat{\boldsymbol{z}}_n)] \tag{80}$$

The independently evolving direct IMPES trajectory is used solely for the profile comparison; it is not the reference in this scalar calibration. The displayed coupled trajectories assess solution direction and propagation between successive time steps, but do not independently validate scale recovery from the postselection probability or sign selection based on the residual.

The propagation of finite QPE error into transport can be stated explicitly. Let $\boldsymbol{p}_*^{n+1}$ be the exact solution of the same pressure system assembled from $\boldsymbol{S}_w^n$, and define the formal finite QPE error $\boldsymbol{e}_p^{n+1} = \widetilde{\boldsymbol{p}}^{n+1} - \boldsymbol{p}_*^{n+1}$. If Π_ℓ extracts the lower block of the dilated solution, then:

$$\boldsymbol{e}_p^{n+1} = \Pi_\ell \boldsymbol{e}_z^{n+1} \tag{81}$$

$$\boldsymbol{e}_z^{n+1} = \|\overline{\boldsymbol{b}}_n\|_2 \sum_j \beta_{j,n}\left(\Phi_{j,n}^{(n_p)} - \lambda_{j,n}^{-1}\right)\boldsymbol{v}_{j,n} \tag{82}$$

where $(\lambda_{j,n}, \boldsymbol{v}_{j,n})$ are the eigenpairs of H_n and $\beta_{j,n}$ are the coefficients of the normalized doubled right side. For fixed $\boldsymbol{S}_w^n$, the corresponding interior water flux error is:

$$\delta u_{w,i+1/2}^{n+1} = -\Lambda_{w,i}^n \frac{e_{p,i+1}^{n+1} - e_{p,i}^{n+1}}{\Delta x} \tag{83}$$

and its one step contribution to the saturation error is:

$$\delta S_{w,i}^{n+1} = -\frac{\Delta t}{\phi \Delta x}\left(\delta u_{w,i+1/2}^{n+1} - \delta u_{w,i-1/2}^{n+1}\right) \tag{84}$$

A spatially uniform pressure offset cancels from all pressure differences and hence from the transport update, whereas errors in pressure scale, gradients, and spectral composition perturb the face fluxes. As the direct and hybrid trajectories diverge, saturation differences alter the mobilities and subsequent flow calculations, so later pressure differences reflect both current QPE errors and accumulated transport errors.

The displayed simulator trajectories instead use the global scalar calibration for the same system defined in Eq. (78), which fixes normalization and global phase before the real lower block is extracted.

In the formal interface, HHL is intended to replace the implicit pressure solve in Step 1 of Section 3.2; constitutive evaluation, matrix assembly, preconditioning, pressure recovery, and the explicit saturation update remain classical. In the reported statevector calculations, however, the exact solution of the same dilated system is also evaluated to determine

this global scalar. The numerical workflow therefore does not eliminate a classical pressure solve. Each reported simulator time step comprises five operations.

Hybrid Step 1: Assembly of the pressure system. Evaluate the phase mobilities at $\boldsymbol{S}_w^n$ and assemble $A_n \boldsymbol{p}^{n+1} = \boldsymbol{b}_n$.

Hybrid Step 2: Preconditioning and Hermitian embedding. Rebuild the left SPAI W_n, form $\overline{A}_n = W_n A_n$ and $\overline{\boldsymbol{b}}_n = W_n \boldsymbol{b}_n$, and construct H_n.

Hybrid Step 3: Signed HHL solve. Prepare the normalized doubled right side, set ρ_n and C_n by Eq. (72), use $\lambda_{c,n} = C_n$, and apply signed HHL with joint ancilla-$|1\rangle$ and phase-$|0\rangle$ postselection.

Hybrid Step 4: Pressure recovery. Align the normalized state obtained after postselection with the exact solution of the dilated system at the same time step using Eq. (78), and extract $\boldsymbol{p}_u^{n+1}$ from the lower block.

Hybrid Step 5: Saturation update. Update $\boldsymbol{S}_w^{n+1}$ using Eqs. (61) and (62). Let $\widetilde{\boldsymbol{S}}_w^{n+1}$ denote the update before saturation projection. Summing these raw updates cancels all internal water fluxes and gives the discrete water balance:

$$\phi A_c \Delta x \sum_{i=1}^{N} \left(\widetilde{S}_{w,i}^{n+1} - S_{w,i}^{n} \right) = \Delta t \, Q_v \left(1 - f_{w,N}^{n} \right) \tag{85}$$

The prescribed water influx minus the outlet water production rate $Q_v f_{w,N}^n$ equals the raw accumulation before projection. The updated saturation then determines the coefficients of the next pressure system, completing one step of the sequential pressure and saturation workflow. No separate local flux correction is applied before the fluxes computed from pressure enter the saturation update. If the saturation projection changes an entry, the stored saturation also contains the corresponding projection correction, which is not represented by Eq. (85); the identity is therefore not used as numerical evidence of local conservation.

The resulting simulator loop supplies the saturation update with pressure extracted from a signed Hermitian block HHL calculation after preconditioning from the left. The statevector is aligned by a global scalar obtained from the same system, and normal equations are not formed. Section 4 examines the component consistency, directional agreement between pressure solutions, and saturation propagation in this coupling. For the simplified fixed rate problem, these comparisons assess the implemented algebraic interface rather than the necessity of complete field pressure recovery.

4. Numerical experiments

The numerical study has two parts: checks of individual components using canonical benchmark equations, followed by application of HHL coupled with IMPES to water flooding in one dimension. All HHL calculations use an ideal Qiskit statevector simulator, and the numerical study focuses on directional agreement and trajectory propagation in a workflow that uses reference alignment. The updated calculations use the Qiskit Aer statevector backend. The matrix exponential is formed classically as a dense unitary and supplied through a controlled unitary gate. This simulator construction does not provide an efficient sparse block encoding, and the logical qubit counts reported below should not be interpreted as estimates of transpiled hardware resources. For the displayed coupled trajectories, the normalized statevector output is aligned by a global scalar with the exact solution of the current dilated system before it is passed to the transport update. This alignment, which is available only in the simulator, isolates the solution direction and trajectory propagation. The plotted water flooding profiles do not independently validate scale recovery from the postselection probability in Eq. (76) or sign selection based on the residual.

Let the nonzero vectors $\boldsymbol{x}_r$ and $\boldsymbol{x}_q$ denote the classical reference and recovered HHL solutions, respectively. The scale sensitive error and the directional agreement are measured by:

$$E_r = \frac{\|\boldsymbol{x}_q - \boldsymbol{x}_r\|_2}{\|\boldsymbol{x}_r\|_2} \tag{86}$$

$$\mathscr{O}_x = \frac{|\boldsymbol{x}_r^{\dagger} \boldsymbol{x}_q|}{\|\boldsymbol{x}_r\|_2 \|\boldsymbol{x}_q\|_2} \tag{87}$$

The reference is identified case by case. Agreement with a classical discrete solution tests the HHL linear solver output, whereas agreement with an analytical solution also reflects the error of the classical discretization. The overlap $\mathscr{O}_x$ is invariant to global phase and solution norm and is interpreted strictly as a measure of directional agreement.

4.1 Part I: Checks of individual components using canonical benchmark problems

The three cases progressively introduce features relevant to the later application. Poisson supplies a single solve whose Hermitian matrix is passed directly to HHL. Implicit diffusion retains a fixed symmetric positive definite matrix but introduces repeated solves with changing right sides. Implicit upwind advection retains repeated solves but introduces a fixed matrix that is not Hermitian and is treated through normal equations. For each benchmark, the reported spatial resolutions are $(N, n_p) = (8,7)$, $(16,8)$, and $(32,9)$. The Poisson problem is steady and therefore has one profile at each resolution. For the two transient problems, the figure layout places the first computed profile in the left column and the final computed profile in the right column for each value of N.

Poisson benchmark. Consider:

$$-w''(x) = \pi^2 \sin(\pi x), \qquad x \in (0,1) \tag{88}$$

$$w(0) = w(1) = 0 \tag{89}$$

whose exact solution is $w(x) = \sin(\pi x)$. On the N interior points $x_i = ih$, $h = 1/(N+1)$, second-order central differences give:

$$A_{\mathrm{P}} \boldsymbol{w} = \boldsymbol{b}_{\mathrm{P}} \tag{90}$$

$$A_{\mathrm{P}} = \begin{pmatrix} 2 & -1 & & \\ -1 & 2 & \ddots & \\ & \ddots & \ddots & -1 \\ & & -1 & 2 \end{pmatrix}, \quad (b_{\mathrm{P}})_i = h^2 \pi^2 \sin(\pi x_i) \tag{91}$$

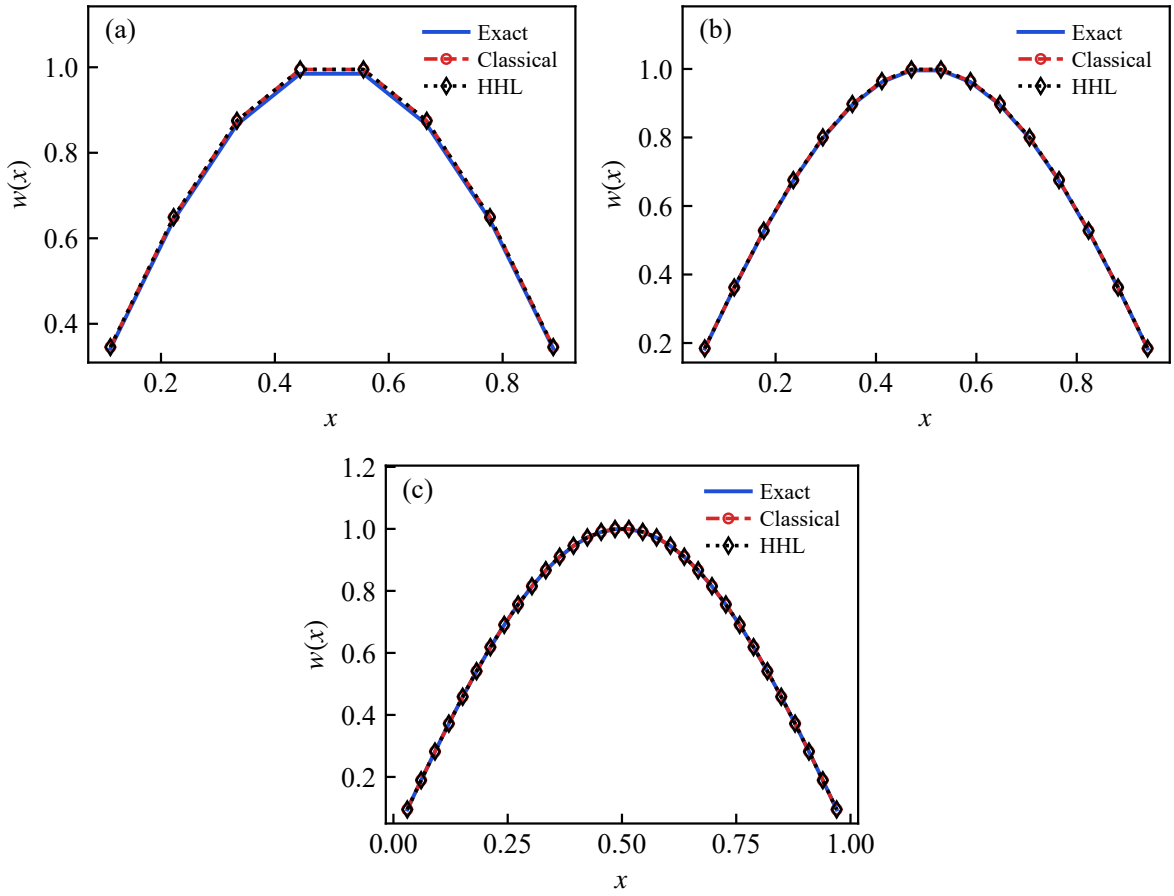


Fig. 3. Single mode Poisson comparison among the analytical, finite difference, and HHL profiles: (a) $(N, n_p) = (8,7)$, (b) $(16,8)$, and (c) $(32,9)$. The prescribed boundary values are included for display, while N counts interior unknowns.

where $\boldsymbol{w} = (w_1, \ldots, w_N)^T$. The matrix A_{P} is symmetric positive definite and can be supplied directly to HHL. Fig. 3 compares the analytical samples, central difference solution, and HHL output at the three reported resolutions.

Let $\boldsymbol{w}_e$ denote the vector of analytical samples, with entries $w_{e,i} = \sin(\pi x_i)$. These samples form exactly one eigenmode of the discrete Laplacian, and:

$$A_{\mathrm{P}}\boldsymbol{w}_e = [2 - 2\cos(\pi h)]\,\boldsymbol{w}_e \tag{92}$$

$$\boldsymbol{w}_h = \frac{h^2\pi^2}{2 - 2\cos(\pi h)}\,\boldsymbol{w}_e \tag{93}$$

The relative errors of 0.0102, 0.0029, and 0.0008 for $N = 8$, 16, and 32, respectively, are finite difference errors relative to the analytical samples rather than discrepancies between the HHL and finite difference solutions. The right side excites only this eigenmode, so the normalized HHL output remains in the same eigendirection and has unit overlap at the displayed precision for all three resolutions. This checks the Hermitian case with a single eigenmode; the diffusion benchmark next extends the calculation to two spectral components.

Diffusion benchmark. On the same grid with N interior points, consider the diffusion equation:

$$\frac{\partial w}{\partial t} = \mathscr{D}\frac{\partial^2 w}{\partial x^2}, \qquad x \in (0,1), \quad t > 0 \tag{94}$$

$$w(0,t) = w(1,t) = 0 \tag{95}$$

where $\mathscr{D} > 0$ is the diffusion coefficient. The benchmark sets $\mathscr{D} = 1$, uses $\Delta t = 0.01$ for five time steps, and takes:

$$w(x,0) = \sin(\pi x) + \sin(2\pi x) \tag{96}$$

with the analytical solution:

$$w(x,t) = \sin(\pi x)e^{-\mathscr{D}\pi^2 t} + \sin(2\pi x)e^{-4\mathscr{D}\pi^2 t} \tag{97}$$

Backward Euler in time and centered differences in space produce:

$$D\boldsymbol{w}^{n+1} = \boldsymbol{w}^n \tag{98}$$

$$D = \mathrm{tridiag}(-\beta_D, 1 + 2\beta_D, -\beta_D) \tag{99}$$

$$\beta_D = \frac{\mathscr{D}\Delta t}{h^2} \tag{100}$$

where $\boldsymbol{w}^n = (w_1^n, \ldots, w_N^n)^T$. The matrix D is symmetric positive definite and remains fixed, whereas the right side changes between the five solves. The initial condition consists of two discrete Laplacian modes, so this case exercises reciprocal weighting across two spectral components rather than the single component in the Poisson problem. Fig. 4 uses a

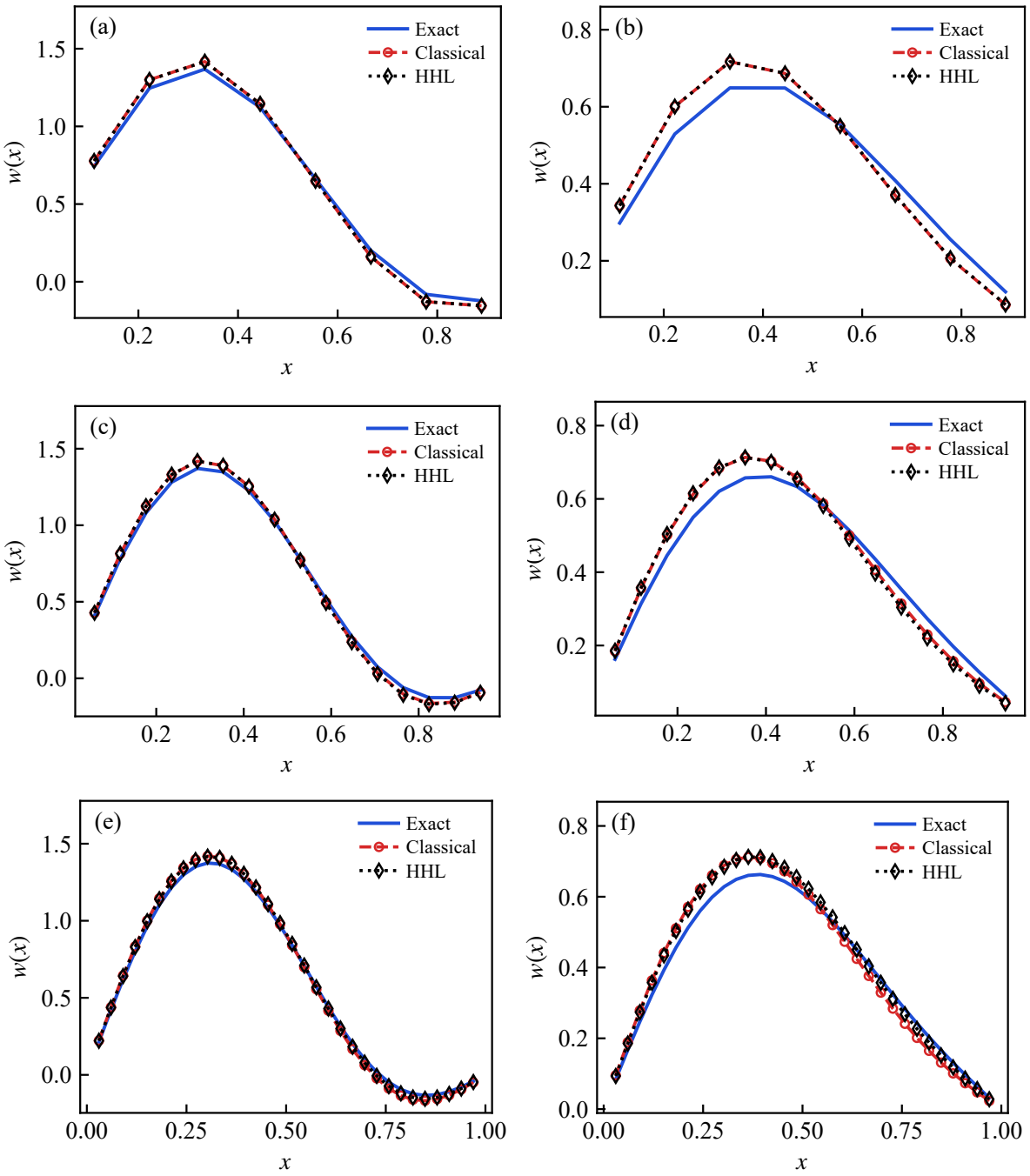


Fig. 4. Comparison for implicit diffusion at the first and final computed time levels: (a) $(N, n_p) = (8, 7)$ at $t = 0.01$, (b) $(8, 7)$ at $t = 0.05$, (c) $(16, 8)$ at $t = 0.01$, (d) $(16, 8)$ at $t = 0.05$, (e) $(32, 9)$ at $t = 0.01$, and (f) $(32, 9)$ at $t = 0.05$.

common three by two layout for the first and final profiles in the sequence of repeated solves.

Across all three grids, the HHL profiles follow the corresponding backward Euler solutions at the first and fifth solves, and the $N = 32$ case shows a more visible difference between the HHL and classical solutions at $t = 0.05$. For the fixed time step used here, $\kappa_2(D)$ increases from 3.77 to 11.35 and 40.47 as N increases from 8 to 16 and 32. The condition number grows by more than a factor of two at each refinement while n_p increases by only one. This unequal scaling means that $\Delta\lambda/\lambda_{\min}$ is not held fixed and reciprocal resolution of the smallest modes deteriorates. The larger difference after repeated solves, particularly for $N = 32$, is consistent with the accumulation of finite QPE and reciprocal weighting errors. The difference between the analytical and classical curves also contains the temporal and spatial discretization errors of the backward Euler finite difference scheme. This test involving repeated solves with a fixed matrix provides the first intermediate step between the single Poisson solve and the coupled water flooding sequence.

Advection benchmark. Consider advection at constant velocity in one dimension:

$$\frac{\partial w}{\partial t}+c\frac{\partial w}{\partial x}=0,\qquad x\in(0,1),\quad t>0,\quad c>0 \tag{101}$$

with a smooth initial pulse $w(x,0)=w_0(x)$ and a prescribed inflow $w(0,t)=g(t)$ satisfying $g(0)=w_0(0)$. The corresponding characteristic solution is:

$$w_*(x,t)=\begin{cases} w_0(x-ct), & x\geq ct \\ g\left(t-\dfrac{x}{c}\right), & 0\leq x<ct \end{cases} \tag{102}$$

The reported calculation uses $w_0(x)=\exp[-(x-1/2)^2]$ and the compatible inflow $g(t)=\exp[-(ct+1/2)^2]$. The numerical experiment uses $c=1$, $\Delta t=0.01$, and five time steps. On the same N-interior point grid as the preceding benchmarks, $x_i=i\Delta x$ with $\Delta x=1/(N+1)$ and $i=1,\ldots,N$. Let $\nu=c\Delta t/\Delta x$. Backward Euler with a backward upwind difference gives:

$$(1+\nu)w_i^{n+1}-\nu w_{i-1}^{n+1}=w_i^n \tag{103}$$

After moving the known inflow value into the first entry on the right side, the system is:

$$A_{\mathrm{A}}\boldsymbol{w}^{n+1}=\boldsymbol{r}^n \tag{104}$$

$$A_{\mathrm{A}}=\begin{pmatrix} 1+\nu & & & \\ -\nu & 1+\nu & & \\ & \ddots & \ddots & \\ & & -\nu & 1+\nu \end{pmatrix} \tag{105}$$

where $\boldsymbol{w}^n=(w_1^n,\ldots,w_N^n)^T$ and:

$$r_1^n=w_1^n+\nu g(t_{n+1}) \tag{106}$$

$$r_i^n=w_i^n,\quad 2\leq i\leq N \tag{107}$$

The real lower bidiagonal matrix A_{A} is nonsymmetric. The calculations use the normal equations:

$$A_{\mathrm{A}}^TA_{\mathrm{A}}\boldsymbol{w}^{n+1}=A_{\mathrm{A}}^T\boldsymbol{r}^n \tag{108}$$

rather than the Hermitian block formulation in Eq. (28). Fig. 5 uses the same three by two layout for the first and final profiles at the three reported resolutions.

At the first computed time level, the reported overlaps between the HHL and classical solutions are 0.999999, 1.000000, and 1.000000 for $N=8$, 16, and 32, respectively. The separation between the analytical and classical curves reflects numerical diffusion from the implicit upwind discretization rather than the HHL solve. The comparison of the first and final computed profiles provides a check of the recovered classical solution direction based on the profiles. The squaring of the condition number established in Eq. (19) motivates the Hermitian block route used for water flooding.

Building on these component checks, Part II introduces evolving pressure matrices, left preconditioning, Hermitian block embedding, and the exchange of pressure and transport data between successive time steps.

4.2 Part II: Application of coupled HHL and IMPES to water flooding in one dimension

Part II addresses two questions for the coupled HHL and IMPES case with a prescribed rate. The first is how the independently evolving pressure and saturation trajectories behave on the three coupled grids under a matched phase register policy. The second is how recycling compares with rebuilding in an independent right SPAI/SAM pilot covering five steps. The direct IMPES workflow provides the classical reference. The two workflows share the physical parameters, boundary conditions, discretization, and initial saturation, but after the first update each branch assembles its next matrix and right side from its own saturation state. Their later differences therefore combine the discrepancy in the current pressure solve with errors accumulated during earlier transport updates. This comparison of coupled trajectories is distinct from a comparison of linear solvers using identical matrices.

The coupled study pairs $(N,n_p)=(8,9)$, $(16,10)$, and $(32,11)$, so that $n_p-\log_2 N=6$ remains fixed. The corresponding Hermitian block systems have dimensions 16, 32, and 64 and require four, five, and six system register qubits, respectively. Including the phase register and the rotation ancilla, the ideal circuits contain 14, 16, and 18 logical qubits before transpilation. The corresponding exhaustive angle tables contain 512, 1024, and 2048 entries, of which at most 511, 1023, and 2047 are nonzero after excluding the zero bin; these are simulator lookup sizes rather than decomposed gate counts. The left SPAI is rebuilt at every coupled pressure step. All runs apply the spectral policy in Eq. (72) at each step and exclude the zero bin. Raw postselection probabilities should not be interpreted as independent measures of accuracy or conditioning because C_n contains an explicit 2^{-n_p} factor and $\|H_n\|_2$ can differ after the trajectories separate.

The calculation uses $L=64$ cm, $\Delta x_N=L/N$, $A_c=10$ cm^2, $Q_v=0.1$ cm^3 s^{-1}, $\phi=0.3$, $k=1$ D, $\mu_w=1$ cP, $\mu_o=2$ cP, $p_L=1$ atm, $S_{wc}=0.2$, $S_{or}=0.35$, $k_{rw}^0=0.3$, $k_{ro}^0=0.8$, and $\eta_w=\eta_o=2$. The matrices are assembled using the stated system of laboratory units and the fixed boundary row normalization of A_n; the reported spectral quantities therefore refer to that explicit algebraic scaling. To provide a common time horizon for comparison, the analysis uses the first 700 time steps of each paired trajectory with $\Delta t=1$ s, and profiles are sampled every 100 steps. Relative permeabilities are tabulated at 50 uniformly spaced saturation values over $[S_{wc},1-S_{or}]$ and linearly interpolated within that interval; queries outside it use the corresponding endpoint table value. Both trajectories use the same saturation bounds after each update.

Study of grid size under a matched phase register policy. Fig. 6 displays the stored pressure and saturation profiles every 100 s through $t=700$ s. Both N and n_p change, so this comparison probes grid size sensitivity under the stated register policy; it is not a pure study of QPE resolution. The profiles compare independently evolving trajectories within the coupled workflow. They do not independently validate normalization and sign recovery because the global scalar is imposed using the solution of the same system; nor do they quantify original system residuals or local flux conser-

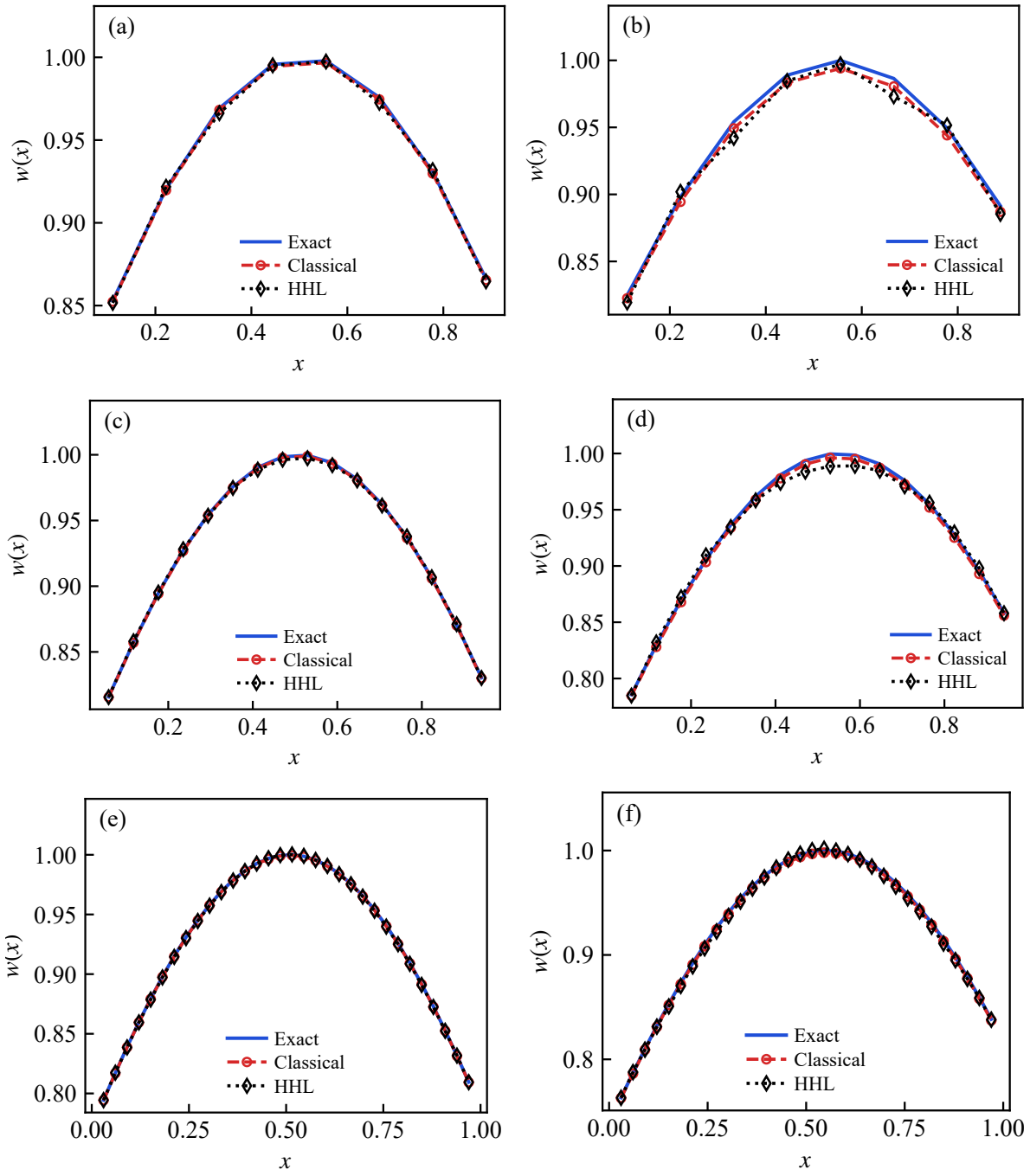


Fig. 5. Implicit upwind advection of a smooth pulse at the first and final computed time levels: (a) $(N, n_p) = (8, 7)$ at $t = 0.01$, (b) $(8, 7)$ at $t = 0.05$, (c) $(16, 8)$ at $t = 0.01$, (d) $(16, 8)$ at $t = 0.05$, (e) $(32, 9)$ at $t = 0.01$, and (f) $(32, 9)$ at $t = 0.05$. HHL is applied to the normal equation systems.

vation. Across the 700 pairs of pressure fields at matched time levels from the independently evolving statevector and direct trajectories, the mean directional overlaps from Eq. (87) are 0.999997, 0.999987, and 0.999917 for $N = 8$, 16, and 32, respectively; the corresponding minima are 0.999991, 0.999954, and 0.999621. Applying the scale sensitive metric in Eq. (86) at each matched time level and then aggregating the 700 values gives mean (maximum) relative pressure differences of 0.00232 (0.00521), 0.00459 (0.0114), and 0.0134 (0.0322). The corresponding saturation differences are 0.00151 (0.00498), 0.00491 (0.0159), and 0.0261 (0.0430). These are discrepancies between coupled trajectories, not errors obtained by comparing linear solvers for the same system. The reported pressure differences are relative vector 2-norm discrepancies computed from the imposed absolute pressures rather than from pressure drops; the saturation differences are evaluated from the stored states after projection. Their increase across the three configurations, together with the visibly larger finest

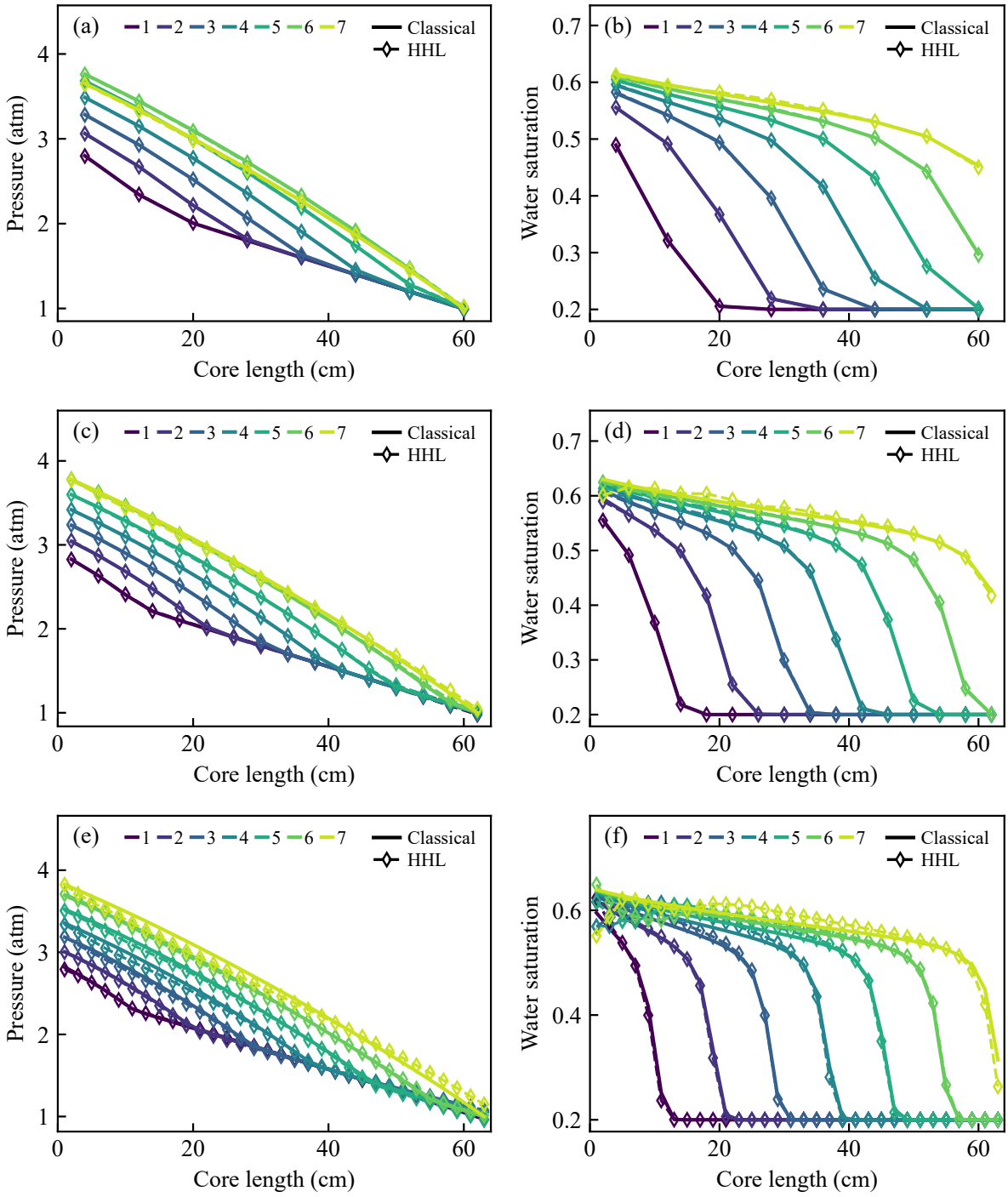


Fig. 6. Pressure (left) and water saturation (right) profiles from independently evolving direct IMPES (solid, Classical) and statevector HHL coupled with IMPES (dashed, open diamonds, HHL) trajectories: (a, b) $(N, n_p) = (8, 9)$, (c, d) (16, 10), and (e, f) (32, 11). Legend numbers 1–7 denote t = 100 to 700 s in steps of 100 s..

grid saturation separation, shows why a pressure overlap close to unity does not by itself establish transport accuracy; the trend combines grid refinement, evolving matrix spectra, phase register resolution, and accumulated trajectory feedback, together with the active projection onto the upper saturation bound during part of the $N = 32$ statevector trajectory.

SPAI rebuilding versus SAM recycling. This study covering five steps is separate from the coupled calculations for different grid sizes. The coupled trajectories use the left SPAI system in Eq. (67), whereas Table 1 uses the right SPAI and SAM definitions in Eqs. (24)-(25). It compares five independently rebuilt right SPAIs with one reference right SPAI followed by four SAM updates for $N = 16$ and $n_p = 9$, using the initial pressure matrix as the SAM reference. For

Table 1. Comparison of SPAI rebuilding and SAM recycling over five steps for $N = 16$ and $n_p = 9$. The timing row includes only preconditioner construction and updating.

Metric	SPAI rebuilt at each step	SAM recycling from initial reference
SPAI computations	5	1
SAM updates	0	4
Total reported setup/update time (s)	0.0020	0.0178
Mean P_1	1.13×10^{-3}	1.15×10^{-3}
Mean pressure overlap	0.99991	0.99987

each path, the reported overlap is the arithmetic mean of the five values obtained from Eq. (87), each evaluated using the pressure from that hybrid path and the pressure from the direct IMPES workflow at the corresponding time. The postselection probability is likewise the arithmetic mean of $P_{1,n}$ over the five solves.

Over the five steps, the rebuilt SPAI and SAM recycling paths yield mean directional overlaps between pressure solutions of 0.99991 and 0.99987, respectively, and mean joint postselection probabilities of 1.13×10^{-3} and 1.15×10^{-3}, respectively. Their reported setup/update totals are 0.0020 and 0.0178 s; these timings cover only preconditioner construction and updating, not the complete coupled workflow. Over five steps, the total setup and update time for SAM recycling is about 8.9 times the corresponding time for rebuilt SPAI in this small $N = 16$ pilot. The two paths retain comparable mean directional overlap between pressure solutions and joint postselection probability, but the timing comparison applies only to this implementation. At $N = 16$, the rebuilt SPAI and each SAM map use tridiagonal factor patterns, so both require columnwise least-squares problems of the same nominal size. After the reference step, both paths solve four further sets of these problems; in the recycling path they determine the SAM maps and are followed by forming or applying $P_n = N_n P_r$. Product formation and other implementation overheads can contribute to the larger recorded total, but no timing breakdown by computational kernel was retained. The observed ratio of 8.9 is therefore reported as a total specific to this implementation rather than an asymptotic property of SAM. Using the two mean probabilities only as representative values, 1.13×10^{-3} and 1.15×10^{-3} correspond to approximately 885 and 870 circuit executions per jointly accepted shot, respectively. By Eq. (18), direct probability sampling to a 5% relative precision in the recovered scale would require approximately 8.8×10^4 and 8.7×10^4 executions before complete field readout. The sampling estimates do not include complete field readout. The pilot covering five steps does not establish performance over a longer period or an advantage in setup time.

5. Conclusion

This work formulates an interface that couples HHL at finite phase resolution with IMPES for a water flooding model in one dimension and studies it with an ideal statevector simulator. Left SPAI and Hermitian block dilation accommodate the selected nonsymmetric boundary row representation. The framework identifies the operations for recovering the scale from the postselection probability, selecting the sign, and reading out the solution on quantum hardware, whereas the displayed coupled trajectories use global scalar calibration based on the same system. They therefore assess directional agreement and data exchange, not independent pressure reconstruction. An equivalent symmetric positive definite pressure system also exists, so the dilation addresses the chosen algebraic representation rather than an intrinsically non-Hermitian physical operator. The Poisson, diffusion, and advection examples provide checks of individual components, and the coupled study compares independently evolving statevector and direct IMPES trajectories for $N = 8$, 16, and 32 under a matched phase register policy. The directional overlap between pressure solutions remains close to one but decreases across the three configurations, while the finest grid profiles show the largest accumulated trajectory discrepancy. The prescribed total rate in the present incompressible case in one dimension makes it a test of the exchange of pressure and transport data between successive time steps; it does not establish that full pressure reconstruction is essential for this simplified physics. A separate right SPAI/SAM pilot covering five steps gives comparable directional agreement between pressure solutions, but its recorded setup/update time is 8.9 times that of rebuilding SPAI and therefore does not demonstrate a timing advantage. All quantum results use direct access to ideal statevector amplitudes; no quantum hardware was used, and no speedup of the complete workflow or hardware advantage is demonstrated.

Acknowledgements

The authors gratefully acknowledge baseline funding from King Abdullah University of Science and Technology and financial support from the National Natural Science Foundation of China (Nos. U24B6001 and 42377138), and the Fundamental Research Funds for the Central Universities (Nos. 25CX02004A and 26CX03002A).

Conflicts of interest

The authors declare no competing interests.

Open Access This article is distributed under the terms and conditions of the Creative Commons Attribution (CC BY-NC-ND) license, which permits unrestricted use, distribution, and reproduction in any medium, provided the original work is properly cited.

References

Aaronson, S. Read the fine print. Nature Physics, 2015, 11: 291-293.

Aziz, K., Settari, A. Petroleum Reservoir Simulation. London, UK, Applied Science Publishers, 1979.

Bai, Y., Hou, J., Liu, Y., et al. Energy-consumption calculation and optimization method of integrated system of injection-reservoir-production in high water-cut reservoir. Energy, 2022, 239: 121961.

Bravo-Prieto, C., LaRose, R., Cerezo, M., et al. Variational quantum linear solver. Quantum, 2023, 7: 1188.

Cai, J., Qin, X., Xia, X., et al. Numerical modeling of multiphase flow in porous media considering micro- and nanoscale effects. Gas Science and Engineering, 2024, 131: 205441.

Cao, Y., Papageorgiou, A., Petras, I., et al. Quantum algorithm and circuit design solving the Poisson equation. New Journal of Physics, 2013, 15: 013021.

Carr, A., de Sturler, E., Gugercin, S. Preconditioning parametrized linear systems. SIAM Journal on Scientific Computing, 2021, 43(4): A2242-A2267.

Chen, H., Sun, S. A new physics-preserving IMPES scheme for incompressible and immiscible two-phase flow in heterogeneous porous media. Journal of Computational and Applied Mathematics, 2021, 381: 113035.

Chen, J., Sun, S., Wang, X. Homogenization of two-phase fluid flow in porous media via volume averaging. Journal of Computational and Applied Mathematics, 2019, 353: 265-282.

Chen, Y., Mao, Y., Yang, L., et al. A comprehensive review of factors affecting dynamic capillary effect in two-phase flow. Transport in Porous Media, 2022, 144(1): 33-54.

Chen, Z. Y., Ma, T. Y., Ye, C. C., et al. Enabling large-scale and high-precision fluid simulations on near-term quantum computers. Computer Methods in Applied Mechanics and Engineering, 2024, 432: 117428.

Childs, A. M., Kothari, R., Somma, R. D. Quantum algorithm for systems of linear equations with exponentially improved dependence on precision. SIAM Journal on Computing, 2017, 46(6): 1920-1950.

Chow, E., Saad, Y. Approximate inverse preconditioners via sparse-sparse iterations. SIAM Journal on Scientific Computing, 1998, 19(3): 995-1023.

Clader, B. D., Jacobs, B. C., Sprouse, C. R. Preconditioned quantum linear system algorithm. Physical Review Letters, 2013, 110: 250504.

Coats, K. H. A note on IMPES and some IMPES-based simulation models. SPE Journal, 2000, 5(3): 245-251.

Dake, L. P. Fundamentals of Reservoir Engineering. Amsterdam, Netherlands, Elsevier, 1978.

El-Amin, M., Kou, J., Sun, S., et al. Adaptive time-splitting scheme for two-phase flow in heterogeneous porous media. Advances in Geo-Energy Research, 2017, 1(3): 182-189.

Ertekin, T., Abou-Kassem, J. H., King, G. R. Basic Applied Reservoir Simulation. Richardson, USA, Society of Petroleum Engineers, 2001.

Evstigneev, N. M., Ryabkov, O. I., Gerke, K. M. Stationary Stokes solver for single-phase flow in porous media: A blastingly fast solution based on algebraic multigrid method using GPU. Advances in Water Resources, 2023, 171: 104340.

Fan, X., Salama, A., Sun, S. A locally and globally phase-wise mass conservative numerical algorithm for the two-phase immiscible flow problems in porous media. Computers and Geotechnics, 2020, 119: 103370.

Gaitan, F. Finding flows of a Navier-Stokes fluid through quantum computing. npj Quantum Information, 2020, 6: 61.

Gerritsen, M. G., Durlofsky, L. J. Modeling fluid flow in oil reservoirs. Annual Review of Fluid Mechanics, 2005, 37: 211-238.

Ghafourpour, L., Laizet, S. Applicability of solving the one- and two-dimensional Poisson equations with the quantum Harrow-Hassidim-Lloyd algorithm. Physical Review Applied, 2025, 24: 024032.

Golden, J., O'Malley, D., Viswanathan, H. Quantum computing and preconditioners for hydrological linear systems. Scientific Reports, 2022, 12: 22285.

Harrow, A. W., Hassidim, A., Lloyd, S. Quantum algorithm for linear systems of equations. Physical Review Letters, 2009, 103: 150502.

He, A., Li, J., Jiang, M., et al. Study of cyclic waterflooding for improving oil recovery in Lukeqin heavy oil reservoir. Geoenergy Science and Engineering, 2023, 223: 211467.

Henderson, J. M., Kath, J., Golden, J. K., et al. Addressing quantum's "fine print" with efficient state preparation and information extraction for quantum algorithms and geologic fracture networks. Scientific Reports, 2024, 14: 3592.

Henderson, J. M., Podzorova, M., Cerezo, M., et al. Quantum algorithms for geologic fracture networks. Scientific Reports, 2023, 13: 2906.

Hui, G., Ren, Y., Bi, J., et al. Artificial intelligence applications and challenges in oil and gas exploration and development. Advances in Geo-Energy Research, 2025, 17(3): 179-183.

Kou, J., Chen, H., Salama, A., et al. An energy stable and positivity-preserving computational method for compressible and immiscible two-phase flow in porous media. Journal of Computational Physics, 2024, 519: 113391.

Kou, J., Wang, X., Chen, H., et al. An energy stable, conservative and bounds-preserving numerical method for thermodynamically consistent modeling of incompressible two-phase flow in porous media with rock compressibility. International Journal for Numerical Methods in Engineering, 2023, 124(11): 2589-2617.

Kou, J., Wang, X., Du, S., et al. An energy stable linear numerical method for thermodynamically consistent modeling of two-phase incompressible flow in porous

media. Journal of Computational Physics, 2022, 451: 110854.

Lake, L. W. Enhanced Oil Recovery. Englewood Cliffs, USA, Prentice Hall, 1989.

Li, J., Zhang, T., Sun, S., et al. Numerical investigation of the POD reduced-order model for fast predictions of two-phase flows in porous media. International Journal of Numerical Methods for Heat and Fluid Flow, 2019, 29(11): 4167-4204.

Liu, P., Jia, C. Dynamic Mohr-Coulomb evaluation of natural fracture stability in deep shale under hydraulic fracturing induced stress superposition. Advances in Geo-Energy Research, 2026, 20(3): 213-226.

Liu, S., Zhang, C., Ghahfarokhi, R. B. A review of lattice-Boltzmann models coupled with geochemical modeling applied for simulation of advanced waterflooding and enhanced oil recovery processes. Energy & Fuels, 2021, 35(17): 13535-13549.

Mattax, C. C., Dalton, R. L. Reservoir Simulation. Richardson, USA, Society of Petroleum Engineers, 1990.

Meena, M. G., Gottiparthi, K. C., Lietz, J. G., et al. Solving the Hele-Shaw flow using the Harrow-Hassidim-Lloyd algorithm on superconducting devices: A study of efficiency and challenges. Physics of Fluids, 2024, 36: 101705.

Meng, X., He, X., Hu, C., et al. A review of parallel computing for large-scale reservoir numerical simulation. Archives of Computational Methods in Engineering, 2025, 32: 4125-4162.

Morales, M. E. S., Pira, L., Schleich, P., et al. Quantum linear system solvers: A survey of algorithms and applications. Reviews of Modern Physics, 2026, 98: 025005.

Nardean, S., Ferronato, M., Abushaikha, A. Linear solvers for reservoir simulation problems: An overview and recent developments. Archives of Computational Methods in Engineering, 2022, 29: 4341-4378.

Nardean, S., Ferronato, M., Abushaikha, A. Block constrained pressure residual preconditioning for two-phase flow in porous media by mixed hybrid finite elements. Computational Geosciences, 2024, 28: 253-272.

Pacheco, T. B., da Silva, A. F. C., Maliska, C. R. Comparison of IMPES, sequential, and fully implicit formulations for two-phase flow in porous media with the element-based finite volume method. Revista Interdisciplinar de Pesquisa em Engenharia, 2017, 2(21): 194-205.

Peaceman, D. W. Fundamentals of Numerical Reservoir Simulation. Amsterdam, Netherlands, Elsevier, 1977.

Qin, X., Xia, Y., Qiao, J., et al. Modeling of multiphase flow in low permeability porous media. Journal of Rock Mechanics and Geotechnical Engineering, 2024, 16(4): 1127-1139.

Saad, Y. Iterative Methods for Sparse Linear Systems, 2nd edition. Philadelphia, USA, Society for Industrial and Applied Mathematics, 2003.

Shayegan, A. H. S. Quantum linear solvers for scientific computing: A comparison of VQLS, HHL and quantum annealing on time-fractional diffusion problems. Scientific Reports, 2026, 16: 10278.

van Essen, G. M., Zandvliet, M. J., Van den Hof, P. M. J., et al. Robust waterflooding optimization of multiple geological scenarios. SPE Journal, 2009, 14(1): 202-210.

Wang, Y., Chung, E. T., Sun, S. Physics-preserving IMPES based multiscale methods for immiscible two-phase flow in highly heterogeneous porous media. Journal of Scientific Computing, 2025, 102: 38.

Wan, Y., Jia, C., Lv, W., et al. Recovery mechanisms and formation influencing factors of miscible CO2 huff-n-puff processes in shale oil reservoirs: A systematic review. Advances in Geo-Energy Research, 2024, 11(2): 88-102.

Willhite, G. P. Waterflooding. Richardson, USA, Society of Petroleum Engineers, 1986.

Wossnig, L., Zhao, Z., Prakash, A. Quantum linear system algorithm for dense matrices. Physical Review Letters, 2018, 120: 050502.

Xu, L., Li, M., Zhang, L., et al. Improved quantum lattice Boltzmann method for advection-diffusion equations with a linear collision model. Physical Review E, 2025, 111: 045305.

Yalovetzky, R., Minssen, P., Herman, D., et al. Solving linear systems on quantum hardware with hybrid HHL^{++}. Scientific Reports, 2024, 14: 20610.

Yang, Y., Horne, R. N., Cai, J., et al. Recent advances on fluid flow in porous media using digital core analysis technology. Advances in Geo-Energy Research, 2023, 9(2): 71-75.

Zhang, Q., Yang, Y., Wang, D., et al. Correlations of residual oil distribution with pore structure during the water flooding process in sandstone reservoirs. Advances in Geo-Energy Research, 2024, 12(2): 113-126.

Zhao, J., Wu, J., Wang, H., et al. Single phase flow simulation in porous media by physical-informed Unet network based on lattice Boltzmann method. Journal of Hydrology, 2024, 639: 131501.

Zhao, L., Feng, C., Zhang, C. S., et al. Parallel multi-stage preconditioners with adaptive setup for the black oil model. Computers & Geosciences, 2022, 168: 105230.

Zou, S., Chen, D., Kang, N., et al. An experimental investigation on the energy signature associated with multiphase flow in porous media. Water Resources Research, 2024, 60(3): e2023WR036241.